Hyperfine-Resolution Mapping of On-Road Vehicle Emissions with Comprehensive Traffic Monitoring and Intelligent Transportation System

Linhui Jiang[1], Yan Xia[1], Lu Wang[1], Xue Chen[1], Jianjie Ye[5], Tangyan Hou[1], Liqiang Wang[1], Yibo Zhang[1], Mengying Li[1], Zhen Li[1], Zhe Song[1], Yaping Jiang[1], Weiping Liu[1], Pengfei Li[3+], Daniel Rosenfeld[4], John H. Seinfeld[2], Shaocai Yu[1,2+]

[1]Research Center for Air Pollution and Health; Key Laboratory of Environmental Remediation and Ecological Health, Ministry of Education, College of Environment and Resource Sciences, Zhejiang University, Hangzhou, Zhejiang 310058, P.R. China
[2]Division of Chemistry and Chemical Engineering, California Institute of Technology, Pasadena, CA 91125, USA.
[3]College of Science and Technology, Hebei Agricultural University, Baoding, Hebei 071000, P.R. China
[4]Institute of Earth Sciences, The Hebrew University of Jerusalem, Jerusalem, Israel
[5]Bytedance Inc., Hangzhou, Zhejiang 310058, China

+*Correspondence to*: Shaocai Yu (shaocaiyu@zju.edu.cn); Pengfei Li (lpf_zju@163.com)

To be submitted to

Atmospheric Chemistry and Physics

Abstract

30   Urban on-road vehicle emissions affect air quality and human health locally and globally. Given uneven sources, they typically exhibit distinct spatial heterogeneity, varying sharply over short distances (10m ~ 1km). However, all-around observational constraints on the emission sources are limited in much of the world. Consequently, traditional emission inventories lack the spatial resolution that can characterize the on-road vehicle emission hotspots. Here we establish a bottom-up approach to reveal a unique pattern of urban on-road vehicle emissions at 1 ~ 3 orders of magnitude higher spatial resolution than current emission

35   inventories. We interconnect all-around traffic monitoring (including traffic fluxes, vehicle-specific categories, and speeds) via an intelligent transportation system (ITS) over the Xiaoshan District in the Yangtze River Delta (YRD) region. This enables us to calculate single-vehicle-specific emissions over each fine-scale (10m ~ 1km) road segment. Thus, the most hyperfine emission dataset of its type is achieved, and on-road emission hotspots appear. The resulting map shows that the hourly average on-road vehicle emissions of CO, NO_x, HC, and $PM_{2.5}$ are 74.01kg, 40.35kg, 8.13kg, and 1.68kg, respectively. More

40   importantly, widespread and persistent emission hotspots emerged. They are of significantly sharp small-scale variability, up to 8 ~ 15 times within individual hotspots, attributable to distinct traffic fluxes, road conditions, and vehicle categories. On this basis, we investigate the effectiveness of routine traffic control strategies on on-road vehicle emission mitigation. Our results have important implications for how the strategies should be designed and optimized. Integrating our traffic-monitoring-based approach with urban air quality measurements, we could address major data gaps between urban air pollutant emissions

45   and concentrations.

1. Introduction

Urban air pollution is a critical risk for premature death globally (Lelieveld et al., 2015; West et al., 2006). A primary reason is the rapid growth in vehicle population for decades, which has led to widespread and severe pollution of fine particulate matter ($PM_{2.5}$) and ozone (O_3) (Anenberg et al., 2017; He et al., 2020; Huang et al., 2020; Kelly and Zhu, 2016; Tessum et al., 2014; Zhang et al., 2012, 2019). Thus, the budget assessment of on-road vehicle emissions is of great significance for air pollution control, epidemiology, exposure assessment, and environmental equity (Anenberg et al., 2017). However, the gradients of on-road vehicle emissions are not well represented in routine emission inventories. The main concern is that the traffic states (e.g., traffic fluxes, road conditions, and vehicle categories) can vary sharply over short distances (10 m ~ 1 km), particularly in urban zones (Chen et al., 2020; Gately et al., 2017; Liu et al., 2019; Wu et al., 2019; Yu et al., 2020).

Routine inventories of on-road vehicle emissions are established based on macro-scale and retrospective statistics. Consequently, they are temporally static for a historical year or month and spatially coarse ($> 1 \times 1 \sim 25 \times 25$ km^2) (Janssens-Maenhout et al., 2015; Li et al., 2017; Zhang et al., 2013). Earlier studies have applied traffic models to improve spatiotemporal resolution (Zhang et al., 2016). However, given that the traffic states were assumed, the simulated emissions were prone to deviate from real-world situations, especially from fine-scale gradients. More importantly, the emission hotspots and their anthropogenic drivers are missed.

Recently, significant advances have been made in comprehensive traffic monitoring techniques. They can help increase the spatiotemporal resolution of traffic states. These methods include GPS-instrumented floating cars (e.g., GPS-equipped probe taxis), open-access congestion maps, radio frequency identification, and traffic video records, each of which has distinct advantages and limitations (Gately et al., 2017; Gately and Hutyra, 2017; Jing et al., 2016; Liu et al., 2018; Wen et al., 2020; Wu et al., 2019; Yang et al., 2019, 2018b). The individual GPS-instrumented floating cars allow us to extrapolate regional-scale vehicle activity levels. Yet, they are relatively scarce compared to the whole fleet, unable to characterize the fine-scale gradients (10m ~ 1km) as well as emission hotspots. Open-access congestion maps typically originate from navigation software, such as Baidu Map. Technically, they collect locations of individual mobile phones as real-time traffic information. On this basis, hierarchical traffic congestion indices can be built up and treated as spatiotemporal surrogates of traffic fluxes and speeds. Despite this, the information for individual vehicles, like speed and categories, remains unavailable. A most recent study (Deng et al., 2020) utilized the BeiDou Navigation Satellite System to develop a full-sample high-resolution emission inventory but only for trucks.

In contrast, comprehensive traffic monitoring technologies, such as radio frequency identification (Paul et al., 2013) coupled with traffic video records (Song et al., 2019), can offer valuable opportunities to fulfill real-time vehicle-specific traffic information. Nevertheless, only in few developed regions, these facilities freshly complete full coverage at a vast expense. Despite this, in the United States, daily traffic activities are released annually at the state-level rather than at high spatiotemporal resolution (hourly and 10m ~ 1km) (Gately et al., 2013). On the other hand, those facilities are inter-

complementary but usually owned and operated by different governmental agencies or private companies separately. Hence, singly relying on either party, hyperfine-resolution emission inventories cannot be derived comprehensively.

80 To this end, it is essential to introduce an intelligent transportation system (ITS) that is capable of interconnecting the independent traffic monitoring and thus offering a complete picture of traffic states (Avila and Mezić, 2020; Yang et al., 2020; Zhang et al., 2018). Hence, this is the unique opportunity to derive a hyperfine-resolution on-road vehicle emission inventory. However, for most developing regions, especially in populous parts of Asia and Africa, such an integrated system is largely absent.

85 As one of the most developed regions in the Yangtze River Delta (YRD), the Xiaoshan District is confronting severe air pollution, particularly with surface O_3 frequently exceeding air quality standards in summertime (http://www.cnemc.cn/). This indicates the significance of mitigating on-road vehicle emissions. Moreover, it is one of the few representatives, in which comprehensive traffic monitoring realizes full coverage and is interconnected via an ITS (named "City Brain") since 2017 (Fig. 1) (Hua, 2018). This allows us to calculate single-vehicle-specific emissions over each fine-scale (10m ~ 1km) road
90 segment. Consequently, we can derive the largest and most hyperfine urban on-road vehicle emission dataset of its type and capture the emission hotspots. Thus, fine-scale gradients (10m ~ 1km) and hotspots of on-road vehicle emissions are exposed. Furthermore, the associated drivers, such as traffic congestion, are further investigated. On this basis, we can directly evaluate the potential impacts of precise (e.g., vehicle-type-specific, road-segment-specific, or traffic-flux-specific) emission mitigation strategies. Our results provide new insights into the spatial variability of urban on-road vehicle emissions.

95 ## 2. Materials and methods

In brief, the objective of this study was to apply a bottom-up model approach to establish a hyperfine-resolution inventory of on-road vehicle emissions over the Xiaoshan District in the YRD (Fig. 1). All key input data, including traffic fluxes, vehicle-specific categories, and speeds, were obtained from comprehensive traffic monitoring coupled with an ITS. Besides, vehicle-specific emission factors came from the local official vehicle Inspect/Maintenance (I/M) dataset, the methodology of which
100 was described in China's National Emission Inventory Guidebook (ICCT, 2020).

2.1. Comprehensive traffic monitoring network

The Xiaoshan District is located in the hinterland of the YRD in China (Fig. 2). In 2019, it had a population of over 1.58 million, 18.56% of the population of New York. Its GDP was close to 200 billion Yuan, ranking fifth among districts in China. The total length of the road network was around 2000 km within a limited geographical extent (i.e., 1417.83 km^2). Under this
105 background, the Xiaoshan District has become an important urban transportation hub in the YRD. Therefore, on-road vehicle emissions were projected to be intensive and play a critical role in affecting fine-scale air quality and exposure equity. Since 2016, routine measures to ease traffic congestion, such as license restrictions during the morning and evening rush hours (from 7:00 to 9:00 and from 16:30 to 18:30, Local Time) on weekdays (i.e., from Monday to Friday), were implemented over the

Xiaoshan District. This would significantly alter fine-scale spatiotemporal patterns of traffic states (including traffic fluxes, vehicle speeds, and fleet compositions) and thus on-road vehicle emissions, but the impacts remain unclear.

2.2. Hyperfine-resolution bottom-up model framework

A hyperfine-resolution bottom-up model framework was established to calculate primary on-road vehicle emissions, including carbon monoxide (CO), hydrocarbon (HC), nitrogen oxides (NO$_x$), and PM$_{2.5}$. Figure 1 is a flow diagram to illustrate the overall methodology for this framework. The results depended on an ensemble calculation of traffic fluxes, road segments, vehicle-specific speed, categories, and emission factors (Eq. 1) (Wu et al., 2019; Yang et al., 2019; Zhang et al., 2016):

$$E_{h,j,l} = \sum_t EF_{c,j}(v) \times TF_{c,h,l} \times L_l, \text{ (Eq. 1).}$$

$E_{h,j,l}$ is the consequent emission of the pollutant j on the road link l at the hour h, the unit of which is grams per hour (g h^{-1}), while the rest variables denote the input data for the model. $EF_{c,j}(v)$ is the average emission factor of the pollutant j for the vehicle category c at the speed v, the unit of which is grams per kilometre (g km^{-1}); $TF_{c,h,l}$ is the traffic flux of the vehicle category c on the road segment l at the hour h, in units of vehicles per hour (veh h^{-1}); L_l is the length of the road segment l in units of kilometres (km).

The major technical advance in this study was that all these input data were vehicle-specific and obtained from all-round traffic monitoring, introduced and detailed in Sect. 2.3. Detailed road segments are important carriers reflecting traffic states and on-road vehicle emissions. In this study, we divided the entire road network over the Xiaoshan District into 1894 road segments. Over the entire district, such road segments were divided into three road classes: highways, arterial roads, and residential streets (Fig. 2). Spatially, each road segment was adaptive to a set of traffic monitoring platforms that can collect comprehensive traffic profiles, including traffic fluxes, vehicle-specific categories, and speeds. Therefore, the all-round traffic monitoring derived the hyperfine-resolution map of road segments and thus $E_{h,j,l}$.

To obtain the key input data for this model, we explored traffic monitoring information that achieved full coverage over the Xiaoshan District (Fig. 2). On this basis, vehicle-specific speed and categories were collected. Besides, the vehicle-category-specific emission factors were obtained from the local official I/M dataset. Consequently, an ITS (named "City Brain") was developed to simultaneously upload the traffic monitoring information and, more importantly, to establish vehicle-specific links between those parameters. Therein traffic fluxes played a major role in affecting vehicle emissions (Deng et al., 2020; Yang et al., 2019). Particularly, traffic congestion in narrow spaces might contribute to urban emission hotspots. To this end, traffic video records, together with image recognition algorithms, were applied to detect vehicle license plates and thus to monitor traffic fluxes. As a result, we constructed a total dataset of 254.31 million records from 13 November 2020 to 13 January 2021. Note that such measurements were recorded by different video facilities and thus of mutually technical barriers. To this end, they were integrated into the ITS and can thus be accessible simultaneously. Besides, accurate vehicle speeds are another key driver that is of great significance for optimizing vehicle emission factors (Yang et al., 2019). In this study, together with traffic fluxes, the vehicle-specific speed was measured concurrently by radar velocimeters. Collectively, a high-resolution

map of traffic states, including traffic fluxes and vehicle-specific speed, was captured by comprehensive traffic monitoring over the Xiaoshan District. From this perspective, this work was distinct from previous attempts that introduced spatial surrogates for traffic states (e.g., floating cars and traffic congestion index in open-source maps) to fill the monitoring gaps. Another key input data is the vehicle-specific category that is closely related to vehicle-specific emission factors (Huang et al., 2020). For each vehicle, an image detection technology based on traffic video records was utilized to recognize its license plate and category. According to the license plate, the identified vehicle category would be verified via the I/M data. Herein, six vehicle categories were detected and defined, including light-duty vehicles (LDVs), middle-duty vehicles (MDVs), heavy-duty vehicles (HDVs), light-duty trucks (LDTs), middle-duty trucks (MDTs), and heavy-duty trucks (HDTs). This classification follows the national standard (GA802-2008). The LDVs were all designated as vehicles in a length of ≤6 m and ridership of ≤9. The MDVs and HDVs were of the same length but with different ridership of 10 ~ 19 and >20, respectively. More definitions of the trucks could be found in the national standard profile (GA802-2008).

According to the detected license plates, these vehicles fell into two types: registered vehicles and non-registered ones in the local official I/M dataset. The emission factors of the former were vehicle-category-specific and speed-dependent, obtained from the I/M dataset, while those of the latter were also speed-dependent but vehicle-category-specific averages (Fig. S1). In this study, the detailed species profiles of HC, as well as evaporative HC, were not included. They were sensitive to fuel properties and environmental conditions, which should be developed based on advanced measurements.

2.3. Traffic control strategies

Based on a hyperfine-resolution map of on-road vehicle emissions, the impacts of traffic control measures on vehicle emission reductions can be directly investigated. Here, four scenarios were designed, which were mainly oriented to traffic fluxes and fleet compositions. Therein the key point was to determine how to conduct these strategies spatially and temporally (Table 1). First, the routine scenario (S1) was conducted during the morning and evening rush hours (from 7:00 to 9:00 and from 16:30 to 18:30, Local Time) on weekdays (i.e., from Monday to Friday). It required that vehicles with specific tail numbers of the license plates were prohibited on the arterial and residential roads. For instance, the prohibited tail numbers were 1 and 9 on Monday. Other detailed rules were illustrated in Table 1. Second, similar to but more stringent than the routine scenario (S1), the scenario (S2) adopted the even-odd rule to reduce the traffic fluxes in half at the same space. Third, the truck scenario (S3) oriented at both local registered and non-registered trucks, which were strictly prohibited all day long over the highways. Finally, the G20 scenario (S4) reflected the traffic states during the G20 summit in 2016 over the Xiaoshan District, with much stricter traffic limitations than normal situations (Ji et al., 2018; Wang et al., 2020; Zhang et al., 2020). It can be regarded as the combination of the scenario (S2) and the truck scenario (S3). That is, all kinds of vehicles should comply with the even-odd rule over the entire district.

2.4. Monte Carlo subsampling

As illustrated above, the hyperfine bottom-up model was a big-data-driven framework. We should thus apply a subsampling analysis to evaluate the stability of the resulting on-road vehicle emission inventory. The objective was to investigate whether less repeated traffic monitoring information can reproduce the long-term spatial emission patterns driven by the entire dataset (Apte et al., 2017; Hankey and Marshall, 2015). For this study, a specific doubt of interest was whether there was a tipping point, beyond which additional information offered relatively little added benefits.

Here we focused only on weekdays rather than weekends when the expected casual trips might affect the analysis. We utilized the Monte Carlo simulations to subsample the full-traffic-monitoring-driven emissions repeatedly. Briefly, we randomly sampled the emission information in unique weekdays ($1 \leqslant N \leqslant 42$) at each road segment from our universal dataset. Each road segment has 35 weekdays of sampling on average. For each value of N, we performed 1000 random draws to generate 10000 subsampled "maps" of fine-scale hourly average emissions. For road segments with fewer than N days of sampling, the "subsampling" effectively contained all data. Consequently, the subsampled maps converged to the full-data-driven results, since N approached the total number of full traffic monitoring information.

We adopted three metrics to compare the performance of each subsampled emission map to that of the full-data-driven result. First, as a metric of precision, we calculated the γ^2 between each subsampled map and the corresponding full data set. The second metric was the normalized root-mean-square error (i.e., the coefficient of variation of the RMSE, CVRMSE). Third, as a metric of the temporal stability of subsampled spatial patterns, we calculated the intraclass correlation (ICC) of each subsampled iteration, grouped by road segments. The ICC is a metric that results from one-way Analysis of Variance (ANOVA) to quantify the degree of similarity among repeated measurements within individual groups (i.e., road segments). After computing the ANOVA for data grouped by road segments, the ICC is calculated as the ratio of the variability between groups (Mean Squares of Treatment/Group, MST) to the sum of the MST and the variability within individual groups (Mean Square Error, MSE):

$$ICC = \frac{MST}{MST+MSE} \text{ (Eq. 2)}.$$

ICC is a common evaluation parameters in intra- and inter-rater reliability analyses (Bartko, 1966; Koo and Li, 2016; Shrout and Fleiss, 1979). By definition, a low ICC can relate to the lack of variabilities among sampled subjects, while a high value indicates that substantially more variabilities occur among groups than does within each group. For a hypothetical dataset where all repeated measurements at each location were precisely equal to each other, the ICC would converge to 1.0. In contrast, for a dataset where the concentration variabilities among repeated measures at each individual location are very high relative to the spatial differences in concentration among roads, the ICC would approach 0. Previous studies suggest that ICC values less than 0.5 are indicative of poor reliability, values between 0.5 and 0.75 indicate moderate reliability, values larger than 0.75 indicate good reliability (Bartko, 1966; Koo and Li, 2016; Shrout and Fleiss, 1979). For this application, ICC values of $0.75 \sim 1$ reflected large and systematic spatial differences, with a low residual temporal variability at each location.

3 Results and discussion

3.1 Traffic characteristics and hotspots

Comprehensive traffic monitoring, coupled with the ITS, painted vivid pictures of within-urban traffic states, including traffic fluxes, fleet compositions, and traffic speeds (Figs. 3, 4 and Figs. S2 ~ S5). Remarkable spatiotemporal heterogeneities in fine-scale patterns were revealed. First, most (i.e., > 96.49%) of the traffic fluxes concentrated over the arterial roads and the residential streets rather than the highways (Fig. 3a). Figure 3b illustrates fine-scale variabilities in the traffic fluxes for an indicative ~ 1 km^2 urban zones. Within this small area, the hourly average traffic fluxes varied by more than 15 times. Even within individual roads, they still varied by more than eight times overall. An expected feature throughout the traffic monitoring dataset was the ubiquity of sharp spatial "traffic hotspots" (length < 100 m). Such hotspots were tentatively classified as individual road segments or clusters, where traffic fluxes exceeded the median level over the whole district. Figure 4 confirms potential causes for an indicative set of hotspots via imagery analysis. A uniform explanation was traffic congestion that, however, was resulted from different drivers, such as large traffic fluxes in major arterial roads and their intersections or constructions in the middle of the roads. Such supplement information provides further details on the hotspot identification scheme.

Second, the hourly average traffic fluxes on weekdays were close to those on weekends (Fig. 3 and Fig. S3). Nevertheless, the variation tendencies displayed a distinct picture during different moments between weekdays and weekends (Fig. S2). On weekdays, the diurnal traffic fluxes showed dramatic fluctuations, two peaks at 07:00 and 17:00, obviously related to the morning and evening rush hours. We noted that such temporal peaks enhanced extensive spatial hotspots, spatially consistent with the above hotspots based on the hourly average data but quantitatively more prominent (Fig. 3). This was because that the morning and evening rushes deteriorated the traffic congestion (Fig. 4). By comparison, the variation extent on weekends was slightly lower than on weekdays and the early peak appeared two hours later (Fig. S2). Overall, the maximum peak on weekends barely hit roughly 96.46% of those on weekdays. Spatially, the hotspots of the traffic fluxes on weekdays were mostly consistent with those on weekends but more variable, reflecting frequent casual travels (Fig. S3). Collectively, the fine-scale spatiotemporal patterns of traffic fluxes over the entire district, particularly the hotspots, relied more on those on weekdays.

Third, significantly strong correlations were found between the traffic speeds and fluxes spatially and temporally. Following the traffic fluxes, the simultaneous vehicle-specific speeds fluctuated substantially throughout the day (Fig. S2). When the traffic fluxes peaked at the morning and evening rushes, the vehicle-specific speeds were expected to be at rock bottom. Although the peaks changed from weekdays to weekends, the valleys kept following such peaks. Spatially, the traffic flux hotspots likely determined the traffic speed hotspots, particularly at the morning and evening rush hours (Fig. S4). In contrast, the vehicle categories were independent of the traffic fluxes. Their diurnal variations showed relative stability, even for different road types, after the morning rush hours (Fig. S2 and Fig. 3). On the other hand, the HDVs and HDTs peaked in the early hours of the morning (i.e., from 1:00 to 5:00). Besides, a striking picture lay in the spatial distributions (Fig. 3 and Fig.

S5). The four types of vehicles, including LDVs, MDVs, LDTs, and MDTs, flocked over (98.52%) the arterial and residential roads, while the rest of vehicle categories, i.e., HDVs and HDTs, concentrated over (3.61%) the highways. Figure 3 details fine-scale spatial distributions of HDVs and HDTs for three indicative highway zones (~ 1 km^2). Therein the spatial hotspots

240 scattered extensively. According to the imagery analysis (Fig. 4), the traffic congestion attributed to the large traffic fluxes of HDVs and HDTs should be the unique driver. Therefore, the fleet compositions would also affect emission distributions significantly, particularly over fine-scale zones.

3.2 Characteristics of on-road vehicle emissions

We established a hyperfine-resolution on-road vehicle emission inventory and captured the emission hotspots (Fig. 5 and Fig.

245 S6). Overall, the hourly average emissions were summed up based on the classified roads (Table S1). It was clear that the emission intensities in the arterial roads, residential streets, and highways followed a descending order, although the residential streets were of the longest length and the largest traffic fluxes. The leading cause was the difference in vehicle categories in different road types (Table S1). For instance, we estimated that the hourly average NO$_x$ emission intensities in the arterial roads, residential streets, and highways were 157.76 g/km, 135.22 g/km, and 107.83 g/km, respectively. For the highways, the

250 hourly average traffic fluxes were 10277, accounting for 1.99% of the total amount, while their emissions amounted to more than 2.04 % of the total emissions.

From the temporal perspective, on-road vehicle emissions of CO, HC, NO$_x$, and PM$_{2.5}$ showed similar trends all day (Fig. S7). For instance, the daytime NO$_x$ emissions accounted for approximately 85.90% of the daily total emissions. Moreover, the NO$_x$ emissions varied throughout the day but reach agreement among the different road types (i.e., the arterial roads, residential

255 streets, and highways). Yet, there was an apparent difference between emissions on weekdays and those on weekends. Similar to the temporal variations in the traffic fluxes on weekdays, those in on-road vehicle emissions also peaked at the morning and evening rush hours. In turn, such temporal patterns were indistinct on weekends.

Spatially, the high hourly average emissions with the unprecedented hyperfine resolution spread all over the district (Fig. 5 and Fig. S6). Such spatial pattern was distinct from previous results that generally show decreases from the centre to the

260 periphery with a radiating structure (Jing et al., 2016; Yang et al., 2019). It was mostly associated with the spatial patterns of the traffic fluxes and vehicle categories (Fig. 3 and Fig. S4). Specifically, the high emissions at the centre were mainly attributed to the high traffic fluxes and low traffic speeds. Note that, on the border of the district, the emission intensities in the residential streets far exceeded (> 436.65%) those in the neighbouring highways. This divergence could be interpreted by the spatial emission distributions of different vehicle categories (Fig. 3 and Fig. S5). For instance, the emissions of HDVs and

265 HDTs in the residential streets contributed the most (79.79%), much higher than those (1.34%) in the neighbouring highways.

3.4 Emission hotpots and drivers

The emissions of each pollutant (i.e., CO, HC, NO_x, and $PM_{2.5}$) generally peaked at the major road intersections, leading to the spatial emission hotspots (Fig. 5 and Fig. S6). The highest hourly average emissions occurred at the intersection of two arterial roads (i.e., North Shixin Road and Shanyin Road), where the measurement monitored the largest traffic fluxes (Fig. 3). At broader spatial scales, these hotspot emissions varied substantially among different road types. For instance, the hourly average emissions for the hotspots in Tonghui North Road and Hongda Road (i.e., arterial roads) were approximately consistent with those in Benjing Road and Hongni Road (i.e., residential streets) (Fig. 5 and Fig. S6, arterial roads vs. residential streets: 374.91g/km vs. 216.12g/km CO; 48.90g/km vs. 34.13g/km HC; 180.61g/km vs. 348.38g/km NO_x; 7.41 vs. 15.81g/km $PM_{2.5}$). In contrast, the hotspot emissions in the arterial roads and highways were substantially elevated above the residential levels. For CO, the hotspot emissions in the highways [arterial roads] exceed those on the residential roads by a factor of 2.1 [2.3]; for HC by a factor of 1.4 [2.6]; for NO_x by a factor of 0.9 [1.1]; and for $PM_{2.5}$ by a factor of 0.8 [1]. Therein, emission hotspots for a given highway road were typically intensive and evident in several areas of the Xiaoshan District (Fig. 5). For instance, we estimated consistently higher (1.2 ~ 2 times) emission levels on a highway (i.e., Airport Road) than those on the neighbouring residential street (i.e., Wenming Road) (Fig. S8). More importantly, the diurnal emission hotspots kept stable spatially (Fig. S9), the hourly spatial patterns of which were roughly consistent with the hourly average level (Fig. 5 and Fig. S6). However, the emission intensities of the hotspots varied during different moments between weekdays and weekends (Fig. S10). The higher emissions of hotspots typically appeared at 08:00 and 18:00 on weekdays, 2.2 ~ 3.4 times larger than the hourly average level.

The indicative hotspots over the urban zones generally stretched for 100 ~ 200m (Fig. 5). Over the short length of the transects, the hourly average emissions rose and fell more than 2.2 times. From the hotspot cores outwards, the hourly average emissions consistently followed "distance-decay" relationships (Fig. 6). An unconstrained three-parameter exponential model, $E(d) = \alpha + \beta\exp(-3d/k)$, reproduced the emission-distance relationship $E(d)$ with high fidelity ($r^2 = 0.96$). Specifically, the isotropic parameter d reflected the distance to the hotspot cores (m); the background parameter α represented the background emissions far from the hotspots ($d \to 1000$m); the parameter β represented the emission increment resulting from proximity to the hotspots; the decay parameter k governed the spatial scale over which emissions relaxed to α. For all pollutants, estimated values of $(\alpha + \beta)$ approached a constant (1.0), indicating that the combined contribution of the background and the near-hotspot increment approached the hotspot emission levels.

Figure 6 shows the decay patterns of the hourly average emissions over urban zones on weekdays. These results reflected the hourly average emission ratios (normalized at the hourly average emissions of the hotspots) from hotspots outwards as a function of the distance (d). Note that the ratios of the hourly average traffic fluxes and vehicle category proportions were calculated in the same way.

Consistent with expectations about the speed-dependent emission factors (Fig. S1), our estimated distance-decay relationships were sharpest for NO_x, intermediate for HC and $PM_{2.5}$, and most shallow for CO. In theory, comprehensive traffic profiles

underlay the estimated hotspot emissions. To elucidate determinants of the emission hotspot patterns, we mined those traffic data (Fig. 3, Fig. 5, and Fig. S6). As expected, we found that the traffic fluxes largely shaped the spatial emission hotspot patterns over the arterial and residential roads. Besides, the specific vehicle categories (i.e., HDVs and HDTs) also play a key role.

For the emission hotspots in the highways, the traffic fluxes and emissions were both distance-dependent and applicable to the "distance-decay" exponential models, while the vehicle categories were consistently stable (Fig. 6). This proves that the traffic fluxes played a cardinal role in determining the spatial emission hotspot patterns over the highways. In contrast, in the arterial and residential roads, coincident peaks of the specific vehicle categories (i.e., HDVs and HDTs) and traffic fluxes corresponded in space to the emission hotspots (Fig. 6). This reveals that, besides the traffic fluxes, the specific vehicle categories (i.e., HDVs and HDTs) also substantially contributed to the high emissions over the arterial and residential roads.

3.5 Impacts of traffic control scenarios

Four scenarios (i.e., S1 ~ S4) demonstrated substantial impacts of traffic management on spatiotemporal traffic states (Fig. S11). Therein the S1 and S2 scenarios focused on reducing the traffic fluxes, while the S3 and S4 scenarios gave full consideration to not only the traffic fluxes but also the fleet compositions (Table 1). Without strict traffic restrictions, the S1 scenario only reduced the traffic fluxes by 3.82 % and showed no significant effects on the traffic flux hotspots. On this basis, the traffic fluxes were further decreased by 9.56 % under the S2 scenario. Most of the traffic flux hotspots vanished. Under the S3 scenario, the fleet compositions were changed evidently over the highways, where HDTs and HDVs were removed. The S4 scenario combined the exclusive settings in the S2 and S3 scenarios and thus realized their consequences. This scenario achieved further decreases in the traffic fluxes (51.3%).

This study estimated that the daily average on-road vehicle emissions were 3.40 tons for CO, 0.482 tons for HC, 2.306 tons for NO_x, and 0.097 tons for $PM_{2.5}$ (Fig. 7 and Fig. S12). Under the S1 scenario, the daily average emissions decreased by small percentages (i.e., 3.74% for CO, 3.43% for HC, 3.13% for NO_x, and 3.08% for $PM_{2.5}$). Compared with the S1 scenario, the S2 scenario led to significant reductions over the arterial and residential roads (i.e., 9.34% for CO, 8.59% for HC, 7.83% for NO_x, and 7.69% for $PM_{2.5}$). This represents the effects of strictly traffic flux controls on on-road vehicle emissions, particularly over the urban zones. The S3 scenario reveals that the HDVs and HDTs were responsible for a major part (15.94 ~ 57.50%) of CO, NO_x, $PM_{2.5}$, and HC emissions over the highways. On this basis, the S4 scenario adopted comprehensive traffic controls, thus reducing roughly additional emissions (i.e., 50.77% for CO, 67.44% for HC, 82.72% for NO_x, and 84.20% for $PM_{2.5}$). As a result, the emission hotspots over all roads were mostly removed. Note that these traffic control scenarios should also alter other traffic parameters (e.g., vehicle-specific speeds). Hence, to further reproduce the feedbacks of traffic states, we should introduce more realistic experiments.

3.6 Comparison with other inventories

330   The localized emission inventory over the Xiaoshan District is still lacking. MEICv1.3 for 2016 and HTAPv2.2 for 2010, as state-of-the-art conventional emission inventories provide a valuable opportunity to evaluate our results (Fig. S13) (Janssens-Maenhout et al., 2015; Li et al., 2017). It should be noted that the spatial resolution of MEICv1.3 and HTAPv2.2 was roughly 0.25° * 0.25° and 0.1° * 0.1°, respectively. Hence, their total emissions over the Xiaoshan District were re-aggregated with area-weighting. It was clear that the monthly average on-road vehicle emissions in this study were significantly lower than

335   those in MEICv1.3 and HTAPv2.2 (i.e., MEIC:14.8% for CO, 30.1% for HC, 40.1% for NO_x, and 19.7% for $PM_{2.5}$. HTAP: 22.4% for CO, 44.5% for HC, 67.7% for NO_x and 29.1% for $PM_{2.5}$). This could be attributed to the persistent on-road vehicle emission mitigation measures in China. Moreover, owing to the limitation of the spatial resolution, these conventional inventories were incapable of depicting the emission hotspots over the Xiaoshan District. Such limitations could be propagated to previous CTM simulations driven by those conventional inventories, thus unable to reproduce the fine-scale on-road vehicle

340   emissions.

3.7 Stability Analysis

Through systematic subsampling of our weekday emission dataset, we found that 15 ~ 30 weekdays were sufficient to reproduce key spatial patterns with good precision and low bias (Figure 8). The following trends hold: a small number of drive days (N < 5) typically resulted in a poor approximation of long-term spatial patterns from the full data set, with generally low

345   precision (γ^2) and high bias (**CV-RMSE**). However, each additional sampling day resulted in a substantial improvement in γ^2 and **CV-RMSE**.

For our dataset, diminishing returns for improvement in γ^2 set in at 15 ~ 25 drive days, with mean γ^2 for NO_x and $PM_{2.5}$ approaching 0.7 after 15 weekdays, and approaching 0.9 after 30 ~ 35 weekdays. We found that ICC values ranged from 0.72 to 0.91 for all pollutants (Table S2). This indicates that our measurement-based long-term spatial patterns were robust to

350   stochastic variability among those samples. Average values of ICC (Figure S14) were generally high for 10 or fewer weekdays, indicating that stochastic temporal variability from a small number of weekdays did not obscure an overall spatially dominated emission pattern. Note that our sampling was restricted to weekday conditions, while spatial patterns may differ at other times (weekends) due to casual trips. Future work may reveal whether similar scaling considerations hold over a broader range of conditions.

4 Conclusions

This work establishes a hyperfine bottom-up approach to reveal a unique on-road vehicle emission pattern at 1 ~ 3 orders of magnitude higher spatial resolution than current emission inventories. In particular, all-around traffic monitoring (including traffic fluxes, vehicle-specific categories, and speeds) is interconnected via an intelligent transportation system (ITS) over the Xiaoshan District in the Yangtze River Delta (YRD) region. This enables us to calculate single-vehicle-specific emissions over

each fine-scale (10m ~ 1km) road segment. Consequently, the most hyperfine emission dataset of its type is achieved, exposing widespread and persistent emission hotspots. More importantly, this map is of significantly sharp small-scale variabilities, up to 8 ~ 15 times within individual hotspots, attributable to distinct traffic fluxes, road conditions, and vehicle categories. Once all kinds of vehicles comply with the even-odd rule over the entire district, more than 50% of the emissions are reduced. By comparison, our results are lower (> 14.8% ~ 67.7%) than those in the conventional emission inventories (i.e., MEICv1.3 and HTAPv2.2). Through systematic subsampling of our weekday emission dataset, we find that 15 ~ 30 weekdays are sufficient to reproduce key spatial patterns with good precision and low bias.

In our model framework, the traffic fluxes are measured accurately. By comparison, the emission factors are of larger uncertainties. This is because although they are obtained from the local official vehicle Inspect/Maintenance (I/M) datasets, some assumptions are inappropriate. For instance, the emission factors are measured in lab circumstances, possibly unsuitable for real-world conditions (Seo et al., 2021). Besides, they are calculated as a function of the vehicle categories and speeds (Fig. S1), without consideration of fuel-dependent discrepancies. Instead, we assumed that, in this study, HDVs and HDTs are diesel-driven, while other vehicle categories are fueled by gasoline. Also, the effects of vehicle ages were ignored. Such assumptions are consistent with previous studies (Yang et al., 2019; Zhou et al., 2017). Future introductions of constraints via near-road emission measurements would decrease such uncertainties.

This work proposes a straightforward emission model framework that can provide several orders of magnitude more spatial information. As shown in our results, this approach could be extended to nationwide megacities if comprehensive traffic conditions are fully measured and interconnected via the ITS. However, its costs are significantly higher than those of previous attempts. To this end, more flexible data collection from low-cost sensors, such as those on cell phones, taxis, and public transit, could substantially lower the costs of monitoring instruments. Furthermore, advances in open-source traffic platforms that can complete those big data interconnections would further decrease the costs. In addition, as demonstrated in Sect. 3.7, our approach, coupled with data reduction algorithms, might also enable high-resolution emission mappings. This indicates an application potential of our approach for middle-sized and small cities where robust traffic monitoring infrastructures are absent.

Overall, routine accessibility of hyperfine-resolution on-road vehicle emissions could have transformative implications for air pollution control, urban management and policymaking, epidemiology, and public awareness (Daellenbach et al., 2020; Dedoussi et al., 2020; Geng et al., 2019; Nyhan et al., 2016; Yang and Zhang, 2018; Zeger et al., 2000). By pinpointing localized emission hotspots, these data may provide new opportunities for policymakers. Specifically, our results can replace the coarse-grid (> 1 × 1 ~ 25 × 25 km2) emission inventory (Janssens-Maenhout et al., 2015; Li et al., 2017; Zhang et al., 2013) as the input of the CTM. Comparably, the meteorological input should also be hyperfine sufficiently, which thus needs to account for large eddy simulations (e.g., WRF-LES) (Zhong et al., 2020). In so doing, dispersion models (e.g., AERMOD) (Yang et al., 2019), instead of full CTMs (Mehmood et al., 2020; Wong et al., 2012; Yu et al., 2013), are sufficient to resolve street-level gradients of air pollution concentrations. Through combination with CTM outputs and near-road air quality measurements (Apte et al., 2017; Grange et al., 2017; Jiang et al., 2018; Yang et al., 2018), the hyperfine-resolution scanning

of responses of air quality to emissions becomes possible. This would help understand highly nonlinear air pollution mechanisms, such as the O3-VOCs-NOx relationships (Li et al., 2019), and thus optimize mitigation policies. Besides, the resulting hyperfine-resolution maps of air pollutant concentrations can help address exposure misclassifications and even directly alter personal behaviours, such that real-time traffic navigation data can now inform individual driving patterns. In addition, these hyperfine-resolution emission and air quality maps might result in broader societal consequences, including urban land-use decisions, ecological planning, and political economy.

Data availability. Traffic monitoring data and model results are available upon request.

Supplement. The supplement related to this article is available online.

405

Author contributions. S.Y., P.L. conceived and designed the research. L. J. performed model simulations. Y. X., X. C., L. W., and J. Y. conducted data analysis. T. H., L. W., Y. Z., M. L., Z. L., Z. S., Y. J., W. L., D. R., and J. H. S contributed to the scientific discussions. S.Y., P.L., and J. H. S wrote and revised the manuscript.

410   *Competing interests.* The authors declare that they have no conflict of interest.

Acknowledgements. This study is supported by the Department of Science and Technology of China (No. 2016YFC0202702, 2018YFC0213506 and 2018YFC0213503), National Research Program for Key Issues in Air Pollution Control in China (No. DQGG0107) and National Natural Science Foundation of China (No. 21577126 and 41561144004). Pengfei Li is supported 415   by Initiation Fund for Introducing Talents of Hebei Agricultural University (412201904), Hebei Youth Top Fund (BJ2020032), National Natural Science Foundation of China (No. 22006030), and National Innovation Program (202010086003).

References

Anenberg, S. C., Miller, J., Minjares, R., Du, L., Henze, D. K., Lacey, F., Malley, C. S., Emberson, L., Franco, V., Klimont, Z. and Heyes, C.: Impacts and mitigation of excess diesel-related NOx emissions in 11 major vehicle markets, Nature, 420   545(7655), 467–471, doi:10.1038/nature22086, 2017.

Apte, J. S., Messier, K. P., Gani, S., Brauer, M., Kirchstetter, T. W., Lunden, M. M., Marshall, J. D., Portier, C. J., Vermeulen, R. C. H. and Hamburg, S. P.: High-Resolution Air Pollution Mapping with Google Street View Cars: Exploiting Big Data, Environ. Sci. Technol., 51(12), 6999–7008, doi:10.1021/acs.est.7b00891, 2017.

Avila, A. M. and Mezić, I.: Data-driven analysis and forecasting of highway traffic dynamics, Nat. Commun., 11(1), 2090, 425   doi:10.1038/s41467-020-15582-5, 2020.

Bartko, J. J.: The Intraclass Correlation Coefficient as a Measure of Reliability, Psychol. Rep., 19(1), 3–11, doi:10.2466/pr0.1966.19.1.3, 1966.

Chen, J., Li, W., Zhang, H., Jiang, W., Li, W., Sui, Y., Song, X. and Shibasaki, R.: Mining urban sustainable performance: GPS data-based spatio-temporal analysis on on-road braking emission, J. Clean. Prod., 270, 122489, 430   doi:https://doi.org/10.1016/j.jclepro.2020.122489, 2020.

Daellenbach, K. R., Uzu, G., Jiang, J., Cassagnes, L.-E., Leni, Z., Vlachou, A., Stefenelli, G., Canonaco, F., Weber, S., Segers, A., Kuenen, J. J. P., Schaap, M., Favez, O., Albinet, A., Aksoyoglu, S., Dommen, J., Baltensperger, U., Geiser, M.,

El Haddad, I., Jaffrezo, J.-L. and Prévôt, A. S. H.: Sources of particulate-matter air pollution and its oxidative potential in Europe, Nature, 587(7834), 414–419, doi:10.1038/s41586-020-2902-8, 2020.

435 Dedoussi, I. C., Eastham, S. D., Monier, E. and Barrett, S. R. H.: Premature mortality related to United States cross-state air pollution, Nature, 578(7794), 261–265, doi:10.1038/s41586-020-1983-8, 2020.

Deng, F., Lv, Z., Qi, L., Wang, X., Shi, M. and Liu, H.: A big data approach to improving the vehicle emission inventory in China, Nat. Commun., 11(1), 2801, doi:10.1038/s41467-020-16579-w, 2020.

Gately, C. K. and Hutyra, L. R.: Large Uncertainties in Urban-Scale Carbon Emissions, J. Geophys. Res. Atmos., 122(20),

440 11,211-242,260, doi:https://doi.org/10.1002/2017JD027359, 2017.

Gately, C. K., Hutyra, L. R., Wing, I. S. and Brondfield, M. N.: A Bottom up Approach to on-Road CO_2 Emissions Estimates: Improved Spatial Accuracy and Applications for Regional Planning, Environ. Sci. Technol., 47(5), 2423–2430, doi:10.1021/es304238v, 2013.

Gately, C. K., Hutyra, L. R., Peterson, S. and Sue Wing, I.: Urban emissions hotspots: Quantifying vehicle congestion and

445 air pollution using mobile phone GPS data, Environ. Pollut., 229, 496–504, doi:https://doi.org/10.1016/j.envpol.2017.05.091, 2017.

Geng, G., Xiao, Q., Zheng, Y., Tong, D., Zhang, Y., Zhang, X., Zhang, Q., He, K. and Liu, Y.: Impact of China's Air Pollution Prevention and Control Action Plan on $PM_{2.5}$ chemical composition over eastern China, Sci. China Earth Sci., 62(12), 1872–1884, doi:10.1007/s11430-018-9353, 2019.

450 Grange, S. K., Lewis, A. C., Moller, S. J. and Carslaw, D. C.: Lower vehicular primary emissions of NO_2 in Europe than assumed in policy projections, Nat. Geosci., 10(12), 914–918, doi:10.1038/s41561-017-0009-0, 2017.

Hankey, S. and Marshall, J. D.: Land Use Regression Models of On-Road Particulate Air Pollution (Particle Number, Black Carbon, PM2.5, Particle Size) Using Mobile Monitoring, Environ. Sci. Technol., 49(15), 9194–9202, doi:10.1021/acs.est.5b01209, 2015.

455 He, G., Pan, Y. and Tanaka, T.: The short-term impacts of COVID-19 lockdown on urban air pollution in China, Nat. Sustain., 3(12), 1005–1011, doi:10.1038/s41893-020-0581-y, 2020.

Hua, X.-S.: The City Brain: Towards Real-Time Search for the Real-World, in The 41st International ACM SIGIR Conference on Research & Development in Information Retrieval, pp. 1343–1344, Association for Computing Machinery, New York, NY, USA., 2018.

460 Huang, Y., Surawski, N. C., Yam, Y.-S., Lee, C. K. C., Zhou, J. L., Organ, B. and Chan, E. F. C.: Re-evaluating effectiveness of vehicle emission control programmes targeting high-emitters, Nat. Sustain., 3(11), 904–907, doi:10.1038/s41893-020-0573-y, 2020.

ICCT: China's vehicle emissions inspection and maintenance program., 2020.

Janssens-Maenhout, G., Crippa, M., Guizzardi, D., Dentener, F., Muntean, M., Pouliot, G., Keating, T., Zhang, Q.,

465 Kurokawa, J., Wankmüller, R. and others: HTAP_v2. 2: a mosaic of regional and global emission grid maps for 2008 and 2010 to study hemispheric transport of air pollution, Atmos. Chem. Phys., 15(19), 11411–11432, 2015.

Ji, Y., Qin, X., Wang, B., Xu, J., Shen, J., Chen, J., Huang, K., Deng, C., Yan, R., Xu, K. and others: Counteractive effects of regional transport and emission control on the formation of fine particles: a case study during the Hangzhou G20 summit, Atmos. Chem. Phys., 18(18), 13581–13600, 2018.

470   Jiang, Z., McDonald, B. C., Worden, H., Worden, J. R., Miyazaki, K., Qu, Z., Henze, D. K., Jones, D. B. A., Arellano, A. F., Fischer, E. V and others: Unexpected slowdown of US pollutant emission reduction in the past decade, Proc. Natl. Acad. Sci., 115(20), 5099–5104, 2018.

Jing, B., Wu, L., Mao, H., Gong, S., He, J., Zou, C., Song, G., Li, X. and Wu, Z.: Development of a vehicle emission inventory with high temporal–spatial resolution based on NRT traffic data and its impact on air pollution in Beijing – Part 1:

475   Development and evaluation of vehicle emission inventory, Atmos. Chem. Phys., 16(5), 3161–3170, doi:10.5194/acp-16-3161-2016, 2016.

Kelly, F. J. and Zhu, T.: Transport solutions for cleaner air, Science (80-.)., 352(6288), 934 LP – 936, doi:10.1126/science.aaf3420, 2016.

Koo, T. K. and Li, M. Y.: A Guideline of Selecting and Reporting Intraclass Correlation Coefficients for Reliability

480   Research, J. Chiropr. Med., 15(2), 155–163, doi:10.1016/j.jcm.2016.02.012, 2016.

Lelieveld, J., Evans, J. S., Fnais, M., Giannadaki, D. and Pozzer, A.: The contribution of outdoor air pollution sources to premature mortality on a global scale, Nature, 525(7569), 367–371, doi:10.1038/nature15371, 2015.

Li, K., Jacob, D. J., Liao, H., Zhu, J., Shah, V., Shen, L., Bates, K. H., Zhang, Q. and Zhai, S.: A two-pollutant strategy for improving ozone and particulate air quality in China, Nat. Geosci., 12(11), 906–910, 2019.

485   Li, M., Zhang, Q., Kurokawa, J., Woo, J.-H., He, K., Lu, Z., Ohara, T., Song, Y., Streets, D. G., Carmichael, G. R. and others: MIX: a mosaic Asian anthropogenic emission inventory under the international collaboration framework of the MICS-Asia and HTAP, Atmos. Chem. Phys., 17(2), 2017.

Liu, J., Han, K., Chen, X. (Michael) and Ong, G. P.: Spatial-temporal inference of urban traffic emissions based on taxi trajectories and multi-source urban data, Transp. Res. Part C Emerg. Technol., 106, 145–165,

490   doi:https://doi.org/10.1016/j.trc.2019.07.005, 2019.

Liu, Y.-H., Ma, J.-L., Li, L., Lin, X.-F., Xu, W.-J. and Ding, H.: A high temporal-spatial vehicle emission inventory based on detailed hourly traffic data in a medium-sized city of China, Environ. Pollut., 236, 324–333, doi:https://doi.org/10.1016/j.envpol.2018.01.068, 2018.

Mehmood, K., Wu, Y., Wang, L., Yu, S., Li, P., Chen, X., Li, Z., Zhang, Y., Li, M., Liu, W., Wang, Y., Liu, Z., Zhu, Y.,

495   Rosenfeld, D. and Seinfeld, J. H.: Relative effects of open biomass burning and open crop straw burning on haze formation over central and eastern China: Modeling study driven by constrained emissions, Atmos. Chem. Phys., 20(4), doi:10.5194/acp-20-2419-2020, 2020.

Nyhan, M., Grauwin, S., Britter, R., Misstear, B., McNabola, A., Laden, F., Barrett, S. R. H. and Ratti, C.: "Exposure Track"—The Impact of Mobile-Device-Based Mobility Patterns on Quantifying Population Exposure to Air Pollution,

500   Environ. Sci. Technol., 50(17), 9671–9681, doi:10.1021/acs.est.6b02385, 2016.

Paul, J., Malhotra, B., Dale, S. and Qiang, M.: RFID based vehicular networks for smart cities, in 2013 IEEE 29th International Conference on Data Engineering Workshops (ICDEW), pp. 120–127., 2013.

Seo, J., Park, J., Park, J. and Park, S.: Emission factor development for light-duty vehicles based on real-world emissions using emission map-based simulation, Environ. Pollut., 270, 116081, doi:https://doi.org/10.1016/j.envpol.2020.116081, 2021.

Shrout, P. E. and Fleiss, J. L.: Intraclass correlations: Uses in assessing rater reliability., Psychol. Bull., 86(2), 420–428, doi:10.1037/0033-2909.86.2.420, 1979.

Song, J., Zhao, C., Lin, T., Li, X. and Prishchepov, A. V: Spatio-temporal patterns of traffic-related air pollutant emissions in different urban functional zones estimated by real-time video and deep learning technique, J. Clean. Prod., 238, 117881, doi:https://doi.org/10.1016/j.jclepro.2019.117881, 2019.

Tessum, C. W., Hill, J. D. and Marshall, J. D.: Life cycle air quality impacts of conventional and alternative light-duty transportation in the United States, Proc. Natl. Acad. Sci., 111(52), 18490 LP – 18495, doi:10.1073/pnas.1406853111, 2014.

Wang, L., Yu, S., Li, P., Chen, X., Li, Z., Zhang, Y., Li, M., Mehmood, K., Liu, W., Chai, T., Zhu, Y., Rosenfeld, D. and Seinfeld, J. H.: Significant wintertime $PM_{2.5}$ mitigation in the Yangtze River Delta, China from 2016 to 2019: observational constraints on anthropogenic emission controls, Atmos. Chem. Phys. Discuss., 2020, 1–31, doi:10.5194/acp-2020-510, 2020.

Wen, Y., Zhang, S., Zhang, J., Bao, S., Wu, X., Yang, D. and Wu, Y.: Mapping dynamic road emissions for a megacity by using open-access traffic congestion index data, Appl. Energy, 260, 114357, doi:https://doi.org/10.1016/j.apenergy.2019.114357, 2020.

West, J. J., Fiore, A. M., Horowitz, L. W. and Mauzerall, D. L.: Global health benefits of mitigating ozone pollution with methane emission controls, Proc. Natl. Acad. Sci. U. S. A., 103(11), 3988 – 3993, doi:10.1073/pnas.0600201103, 2006.

Wong, D. C., Pleim, J., Mathur, R., Binkowski, F., Otte, T., Gilliam, R., Pouliot, G., Xiu, A., Young, J. O. and Kang, D.: WRF-CMAQ two-way coupled system with aerosol feedback: software development and preliminary results, Geosci. Model Dev., 5(2), 299–312, 2012.

Wu, L., Chang, M., Wang, X., Hang, J. and Zhang, J.: Development of a real-time on-road emission (ROE v1.0)model for street-scale air quality modeling based on dynamic traffic big data, Geosci. Model Dev. Discuss., 1–19, doi:10.5194/gmd-2019-74, 2019.

Yang, B., Zhang, K. M., Xu, W. D., Zhang, S., Batterman, S., Baldauf, R. W., Deshmukh, P., Snow, R., Wu, Y., Zhang, Q., Li, Z. and Wu, X.: On-Road Chemical Transformation as an Important Mechanism of NO_2 Formation, Environ. Sci. Technol., 52(8), 4574–4582, doi:10.1021/acs.est.7b05648, 2018a.

Yang, D., Zhang, S., Niu, T., Wang, Y., Xu, H., Zhang, K. M. and Wu, Y.: High-resolution mapping of vehicle emissions of atmospheric pollutants based on large-scale, real-world traffic datasets, Atmos. Chem. Phys., 19(13), 8831–8843, doi:10.5194/acp-19-8831-2019, 2019.

Yang, J. and Zhang, B.: Air pollution and healthcare expenditure: Implication for the benefit of air pollution control in China, Environ. Int., 120, 443–455, doi:https://doi.org/10.1016/j.envint.2018.08.011, 2018.

535 Yang, W., Yu, C., Yuan, W., Wu, X., Zhang, W. and Wang, X.: High-resolution vehicle emission inventory and emission control policy scenario analysis, a case in the Beijing-Tianjin-Hebei (BTH) region, China, J. Clean. Prod., 203, 530–539, doi:https://doi.org/10.1016/j.jclepro.2018.08.256, 2018b.

Yang, Z., Peng, J., Wu, L., Ma, C., Zou, C., Wei, N., Zhang, Y., Liu, Y., Andre, M., Li, D. and Mao, H.: Speed-guided intelligent transportation system helps achieve low-carbon and green traffic: Evidence from real-world measurements, J.

540 Clean. Prod., 268, 122230, doi:https://doi.org/10.1016/j.jclepro.2020.122230, 2020.

Yu, Q., Zhang, H., Li, W., Song, X., Yang, D. and Shibasaki, R.: Mobile phone GPS data in urban customized bus: Dynamic line design and emission reduction potentials analysis, J. Clean. Prod., 272, 122471, doi:https://doi.org/10.1016/j.jclepro.2020.122471, 2020.

Yu, S., Mathur, R., Pleim, J., Wong, D., Gilliam, R., Alapaty, K., Zhao, C. and Liu, X.: Aerosol indirect effect on the grid-

545 scale clouds in the two-way coupled WRF-CMAQ: model description, development, evaluation and regional analysis, Atmos. Chem. Phys. Discuss., 25649, 2013.

Zeger, S. L., Thomas, D., Dominici, F., Samet, J. M., Schwartz, J., Dockery, D. and Cohen, A.: Exposure measurement error in time-series studies of air pollution: concepts and consequences., Environ. Health Perspect., 108(5), 419–426, doi:10.1289/ehp.00108419, 2000.

550 Zhang, G., Xu, H., Wang, H., Xue, L., He, J., Xu, W., Qi, B., Du, R., Liu, C., Li, Z., Gui, K., Jiang, W., Liang, L., Yan, Y. and Meng, X.: Exploring the inconsistent variations in atmospheric primary and secondary pollutants during the 2016 G20 summit in Hangzhou, China: implications from observations and models, Atmos. Chem. Phys., 20(9), 5391–5403, doi:10.5194/acp-20-5391-2020, 2020.

Zhang, Q., He, K. and Huo, H.: Policy: cleaning China's air, Nature, 484(7393), 161, 2012.

555 Zhang, Q., Zheng, Y., Tong, D., Shao, M., Wang, S., Zhang, Y., Xu, X., Wang, J., He, H., Liu, W., Ding, Y., Lei, Y., Li, J., Wang, Z., Zhang, X., Wang, Y., Cheng, J., Liu, Y., Shi, Q., Yan, L., Geng, G., Hong, C., Li, M., Liu, F., Zheng, B., Cao, J., Ding, A., Gao, J., Fu, Q., Huo, J., Liu, B., Liu, Z., Yang, F., He, K. and Hao, J.: Drivers of improved PM_{2.5} air quality in China from 2013 to 2017, Proc. Natl. Acad. Sci., 116(49), 24463 LP – 24469, doi:10.1073/pnas.1907956116, 2019.

560 Zhang, S., Wu, Y., Liu, H., Wu, X., Zhou, Y., Yao, Z., Fu, L., He, K. and Hao, J.: Historical evaluation of vehicle emission control in Guangzhou based on a multi-year emission inventory, Atmos. Environ., 76, 32–42, doi:https://doi.org/10.1016/j.atmosenv.2012.11.047, 2013.

Zhang, S., Wu, Y., Huang, R., Wang, J., Yan, H., Zheng, Y. and Hao, J.: High-resolution simulation of link-level vehicle emissions and concentrations for air pollutants in a traffic-populated eastern Asian city, Atmos. Chem. Phys., 16(15), 9965–

565 9981, doi:10.5194/acp-16-9965-2016, 2016.

Zhang, S., Niu, T., Wu, Y., Zhang, K. M., Wallington, T. J., Xie, Q., Wu, X. and Xu, H.: Fine-grained vehicle emission management using intelligent transportation system data, Environ. Pollut., 241, 1027–1037, doi:https://doi.org/10.1016/j.envpol.2018.06.016, 2018.

570 Zhong, J., Nikolova, I., Cai, X., MacKenzie, A. R., Alam, M. S., Xu, R., Singh, A. and Harrison, R. M.: Traffic-induced multicomponent ultrafine particle microphysics in the WRF v3.6.1 large eddy simulation model: General behaviour from idealised scenarios at the neighbourhood-scale, Atmos. Environ., 223, 117213, doi:https://doi.org/10.1016/j.atmosenv.2019.117213, 2020.

Zhou, Y., Zhao, Y., Mao, P., Zhang, Q., Zhang, J., Qiu, L. and Yang, Y.: Development of a high-resolution emission inventory and its evaluation and application through air quality modeling for Jiangsu Province, China, Atmos. Chem. Phys.,
575 17(1), 211–233, 2017.
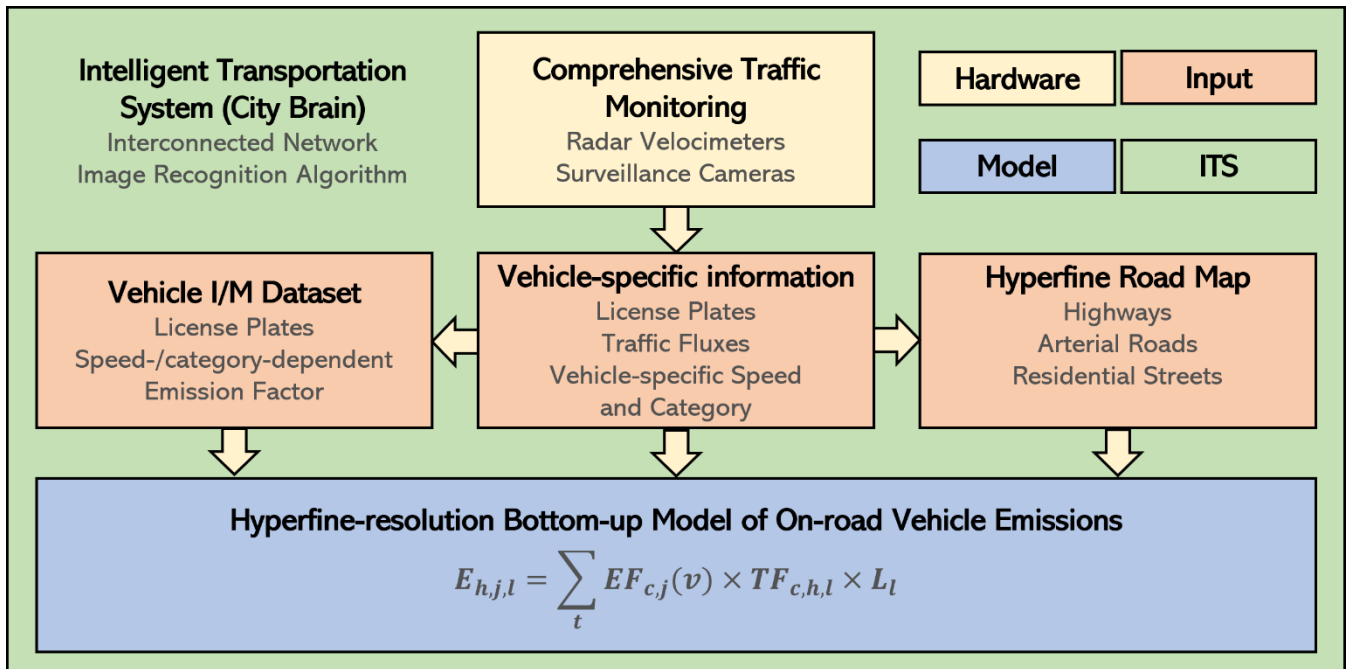
Figure 1. A hyperfine-resolution model framework for on-road vehicle emissions. Traffic monitoring includes radar velocimeters and surveillance cameras. License plates, speed, categories, and traffic fluxes are collected. The speed-/category-dependent emission factors are obtained from the local official vehicle I/M dataset. Road segments are divided into three road classes: highways, arterial roads, and residential streets. An intelligent transportation system (ITS) (named "City Brain") is developed to interconnect these input data. An image recognition algorithm is embedded to recognize the category for a certain vehicle. The detail information is illustrated in Sect. 2.2.
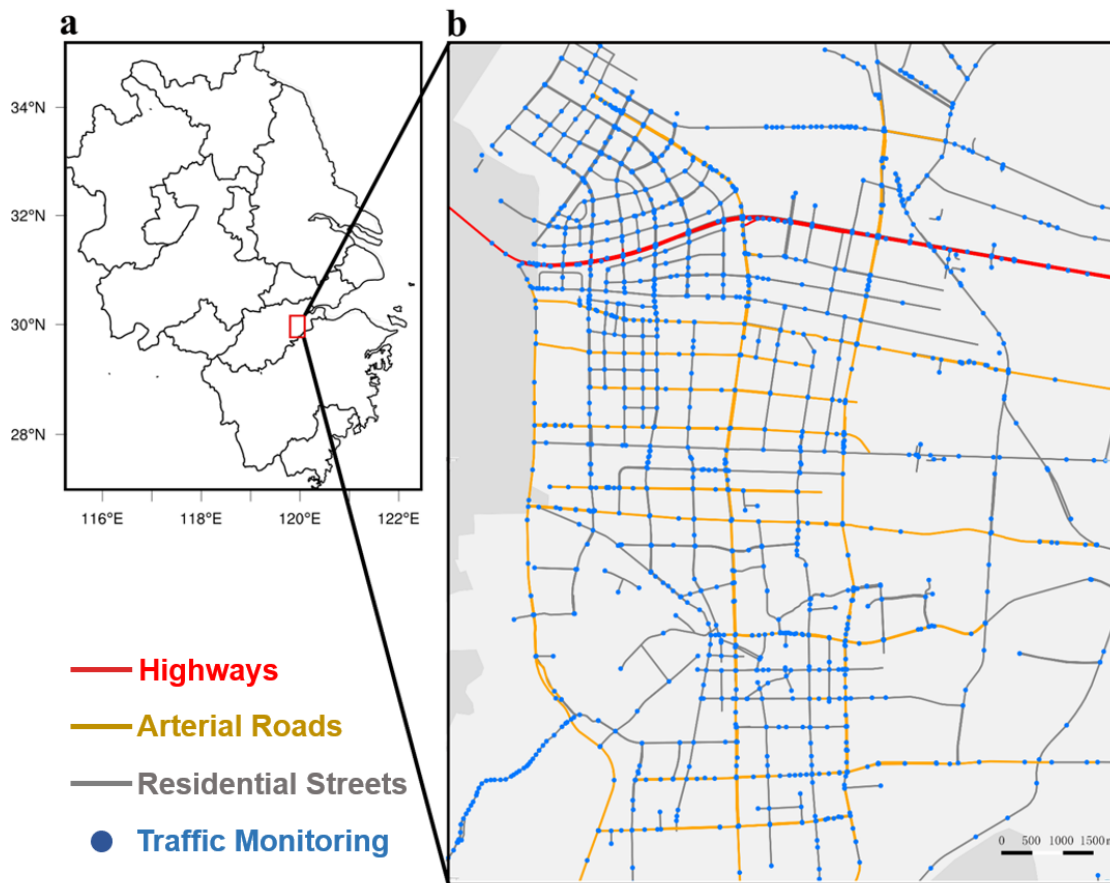
585

Figure 2. Comprehensive traffic monitoring network in the Xiaoshan District. (**a**) The Xiaoshan District (the red rectangle) is located in the hinterland of the YRD in China. (**b**) Comprehensive traffic monitoring achieves full coverage over the Xiaoshan District. Each dot represents a set of comprehensive traffic monitoring that can recognize traffic fluxes, vehicle-specific speed, categories, and license plates. The gaps between two sets, ranging from 10 m to 1 km, determine the spatial resolution of the road

590 and emission map. The entire road network over the Xiaoshan District is divided into 1894 road segments. Such road segments are divided into three road classes: highways (red lines), arterial roads (yellow lines), and residential streets (grey lines). Map data © 2021, Gaode Map.

Traffic fluxes

595
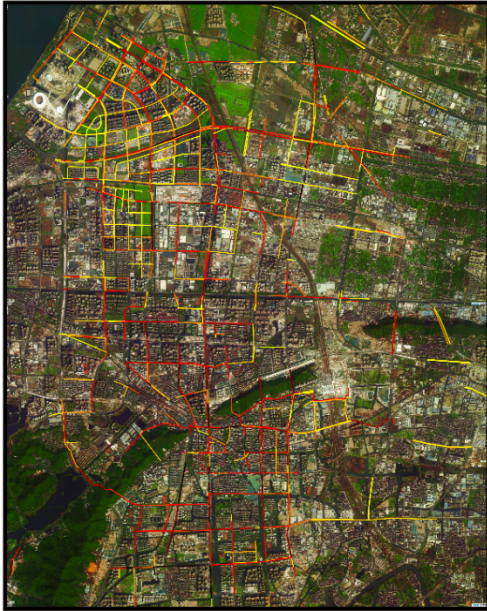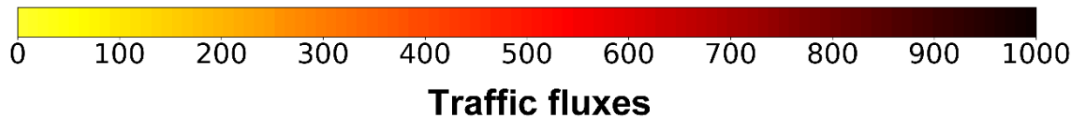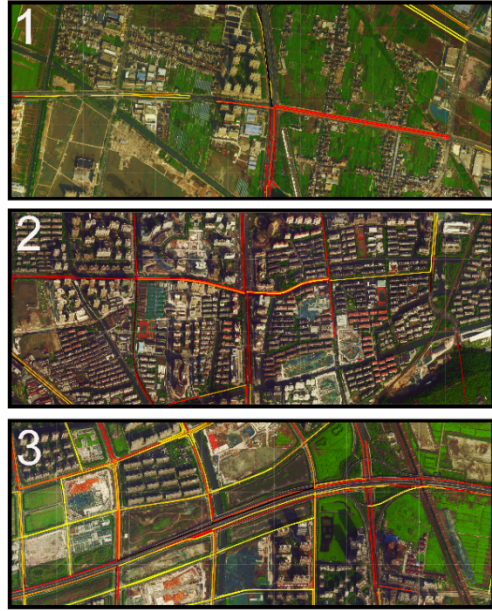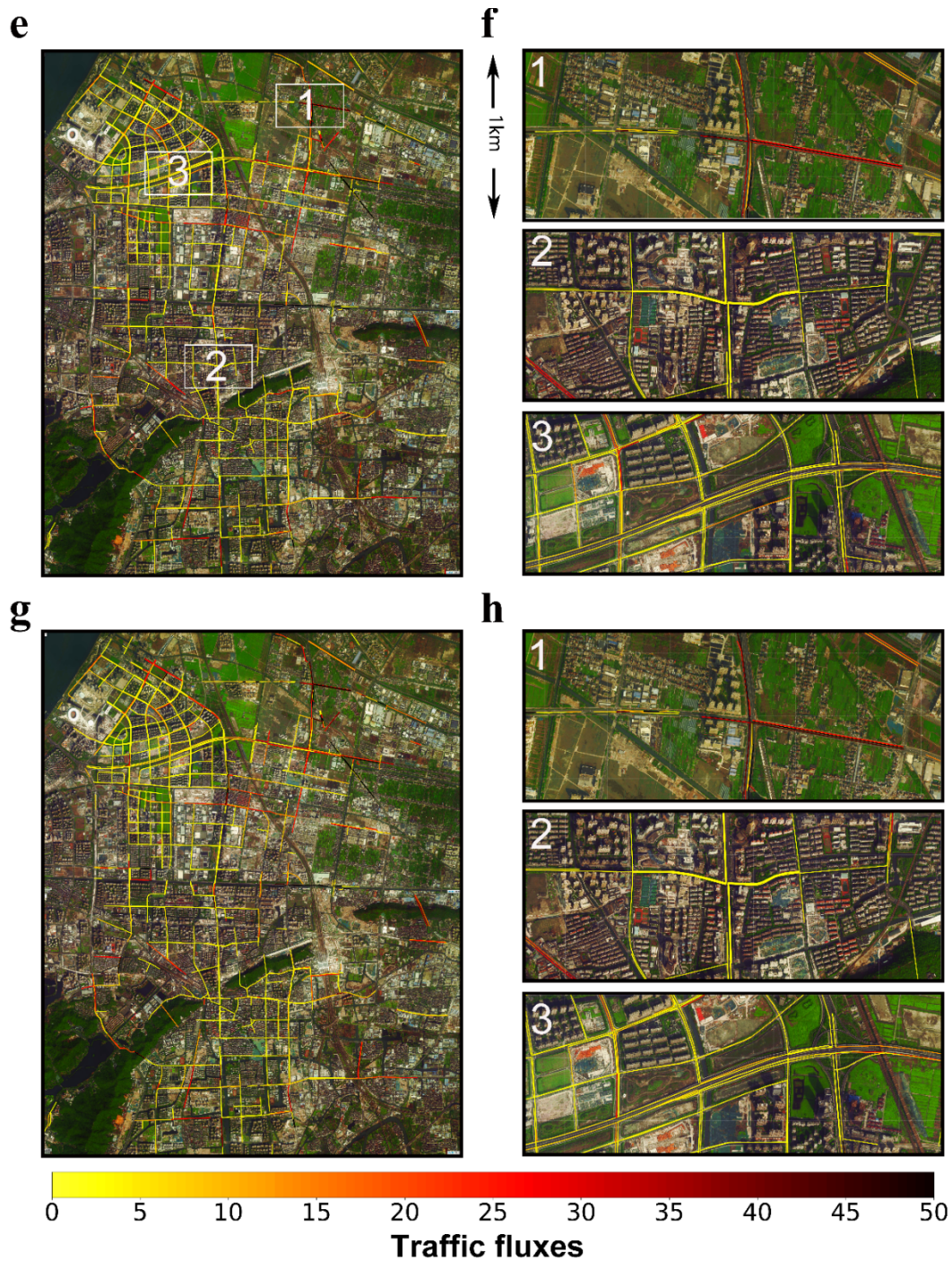
Figure 3. Hyperfine-resolution mapping of observed traffic fluxes. (**a**) Hourly average traffic fluxes in each road segment based on two-month traffic monitoring data over the entire district and (**b**) for three indicative 1 km² urban zones therein. The subgraphs (**c**) and (**d**) are as the same as (**a**) and (**b**) but for the hourly average traffic fluxes during the morning and evening

600   rush hours (from 7:00 to 9:00 and from 16:30 to 18:30, Local Time) on weekdays (from Monday to Friday). The subgraphs (**e**) and (**f**) are as the same as (**a**) and (**b**) but for the hourly average traffic fluxes of HDVs and HDTs. The subgraphs (**g**) and (**h**) are as the same as (**c**) and (**f**) but for the morning and evening rush hours on weekdays. The indicative zones are marked by white rectangles in (**a**) and their spatial scales are presented in (**b**). Illustrative traffic hotspots (circles) are also annotated in (**a**), including Tonghui North Road, Hongda Road, Shixin North Road, Shanyin Road, and Airport Road. Map data © 2021,

605   Gaode Map.

Figure 4. Imagery analysis for illustrative traffic hotspots. (**a ~ b**) Over the hotspots in the urban zones, frequent large traffic fluxes are identified in major arterial roads and their intersections. (**c**) Constructions in the middle of the roads also lead to traffic congestion. (**d ~ e**) Morning and afternoon traffic rushes further deteriorate traffic congestion. (**f**) Over the highways, the hotspots are related to large traffic fluxes of MDTs and HDTs. The vehicle licence plates are pixelated. The hotspot locations are presented in Fig. 3.

e

f

1km

g

h

NO$_X$ (g/km)

0   100   200   300   400   500   600   700
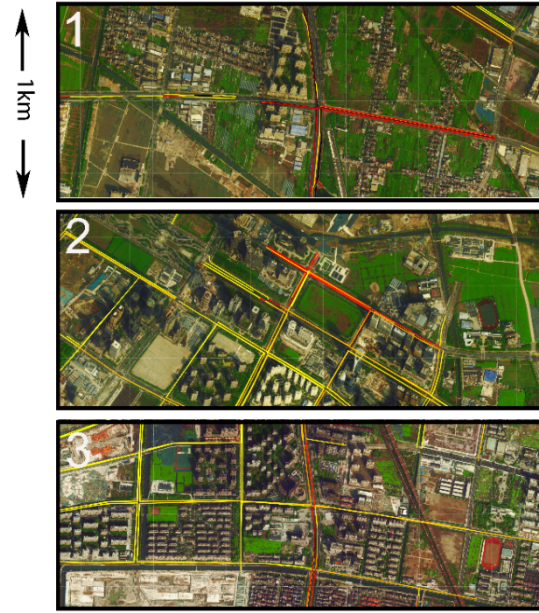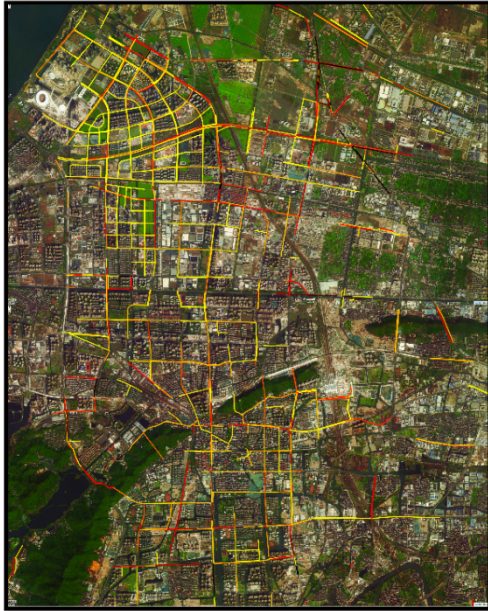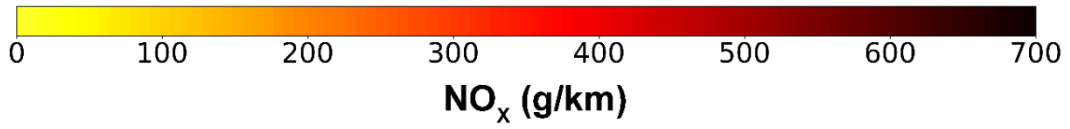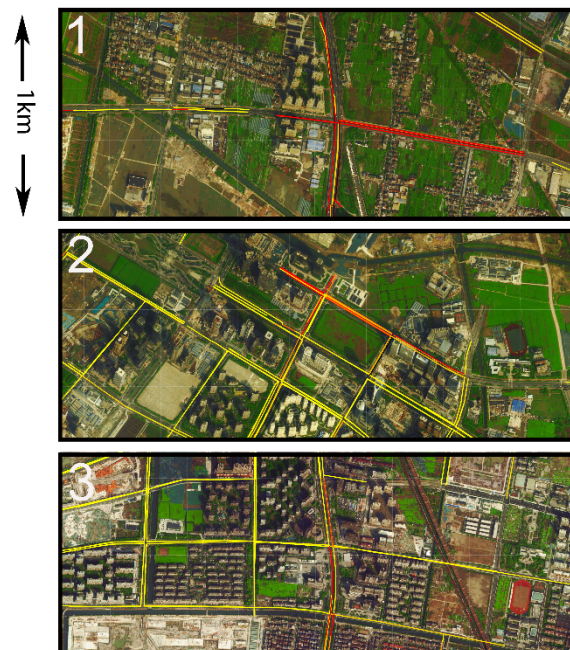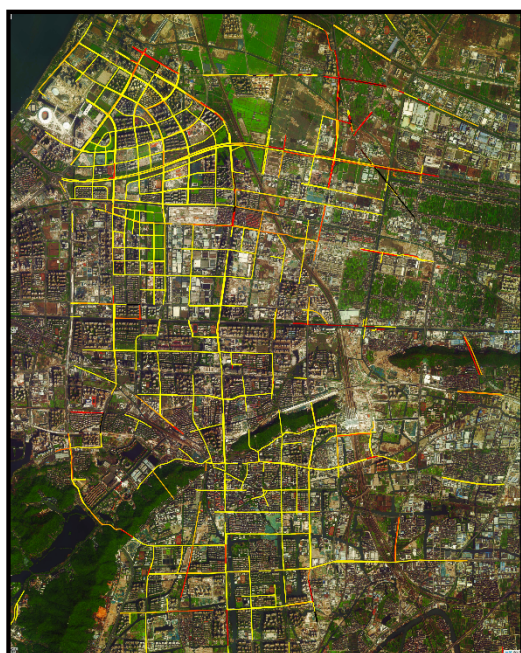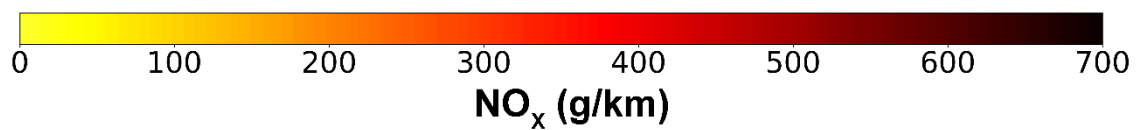
Figure 5. Hyperfine-resolution mapping of on-road vehicle emissions. (**a**) Hourly average on-road vehicle NO_x emissions for each road segment based on two-month traffic monitoring data for the entire district and (**b**) for three indicative 2.5 km^2 urban zones therein. The subgraphs (**c**) and (**d**) are as the same as (**a**) and (**b**) but for the hourly average emissions during the morning and evening rush hours (from 7:00 to 9:00 and from 16:30 to 18:30, Local Time) on weekdays (from Monday to Friday). The subgraphs (**e**) and (**f**) are as the same as (**a**) and (**b**) but for the hourly average emissions of HDTs and HDVs. The subgraphs (**g**) and (**h**) are as the same as (**a**) and (**b**) but for the hourly average emissions of HDTs and HDVs during the morning and evening rush hours on weekdays. The indicative zones are marked by white rectangles in (**a**). Map data © 2021, Gaode Map.
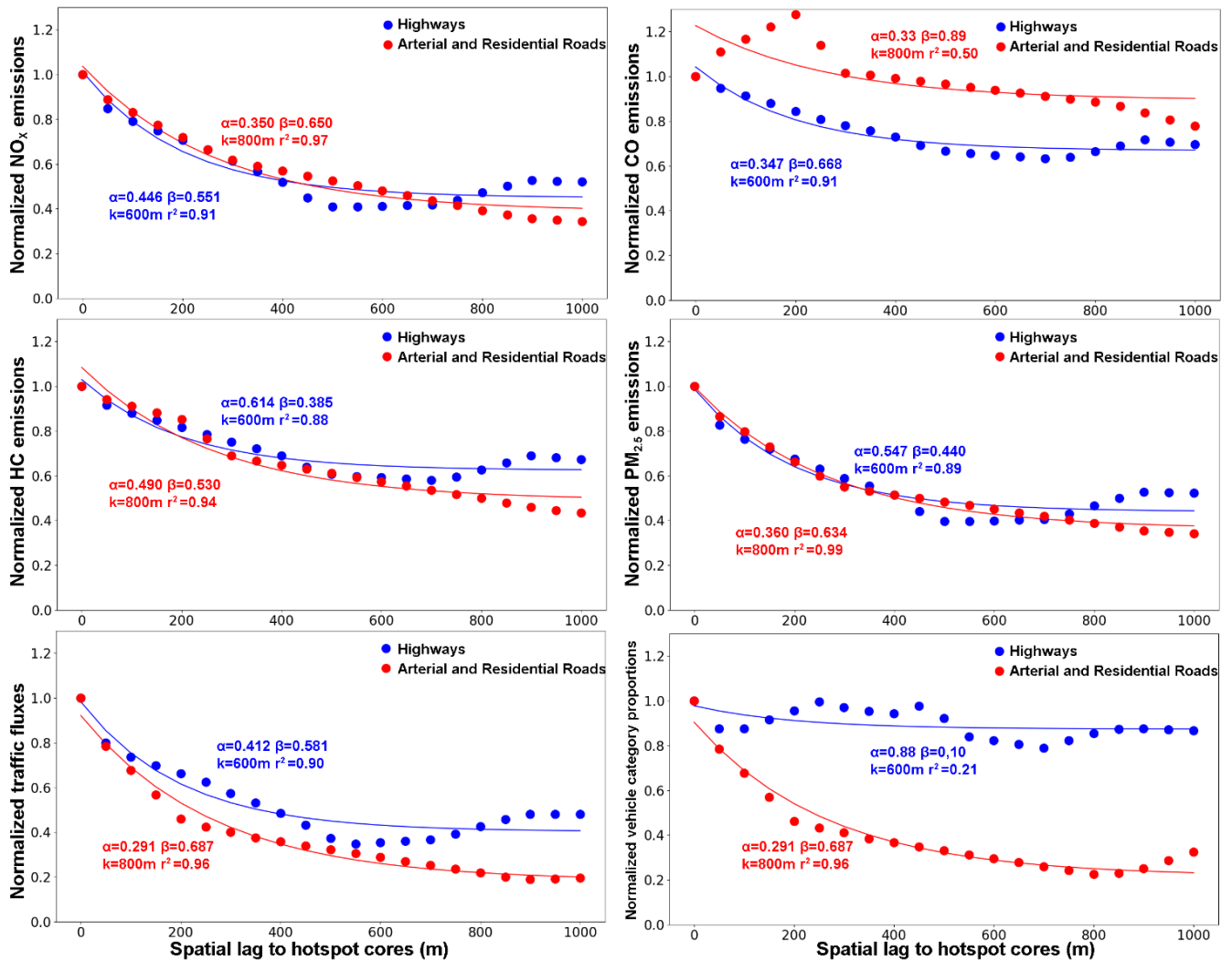
Figure 6. Decay of on-road vehicle emissions, traffic fluxes, and vehicle categories from indicative hotspots outwards on weekdays. (**a ~ d**) Points denote the ratio of hourly average emissions (NO_x, CO, HC, and $PM_{2.5}$) over different road types at a given distance from hotspots to hourly average hotspot emissions. Error bars present standard deviations. An unconstrained three parameter exponential model reproduces the decay relationships with high fidelity. The isotropic parameter d reflected the distance to the hotspot cores (**m**); the background parameter α represented the background emissions far from the hotspots ($d \rightarrow 1000m$); the parameter β represented the emission increment resulting from proximity to the hotspots; the decay parameter k governed the spatial scale over which emissions relaxed to α. The subgraphs (**e**) and (**f**) are the same as (**a**) but for traffic fluxes and the vehicle category proportions, respectively.
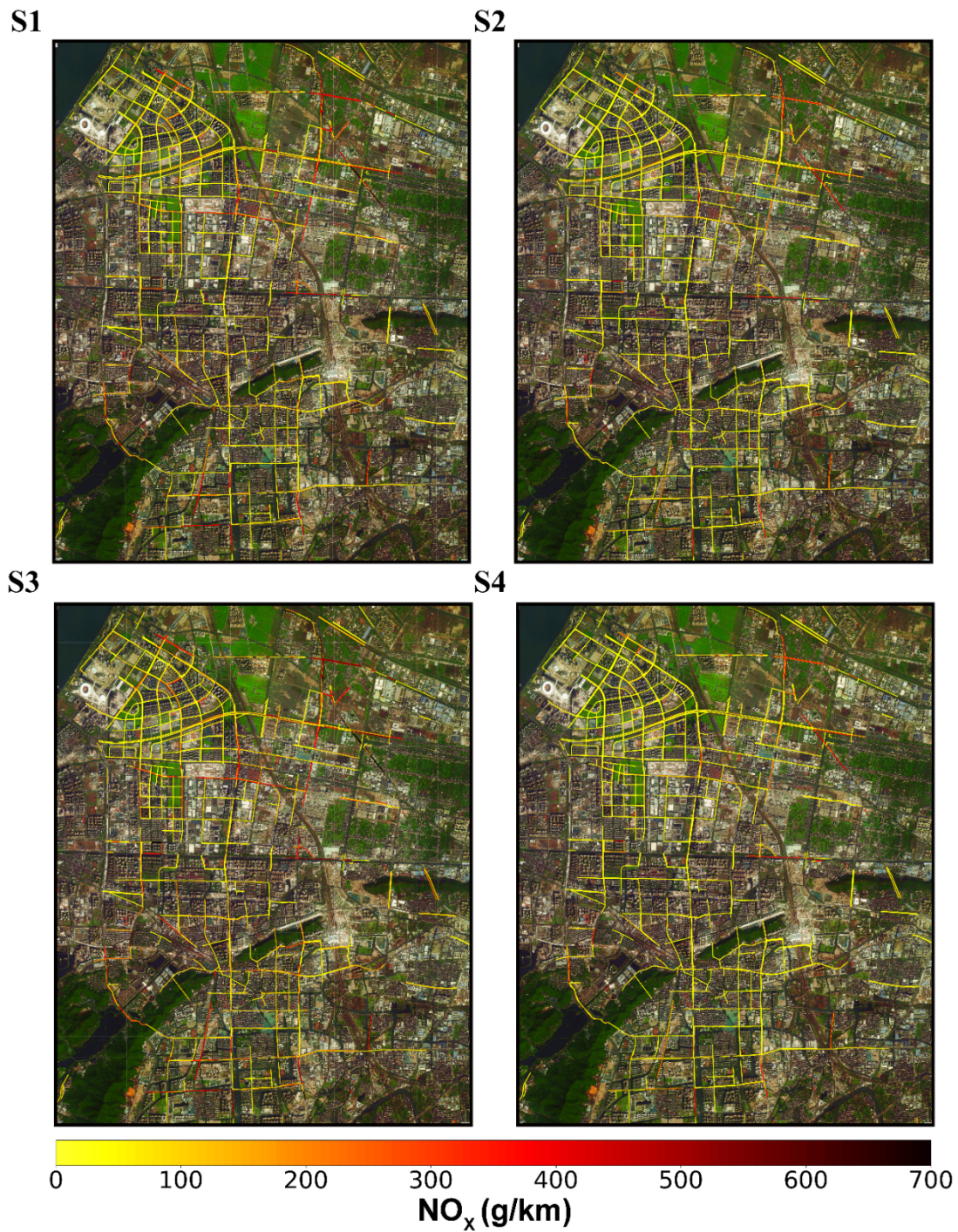
Figure 7. Impacts of traffic control strategies (i.e., S1, ~ S4) on daily average on-road vehicle NO$_x$ emissions. Map data © 2021, Gaode Map.
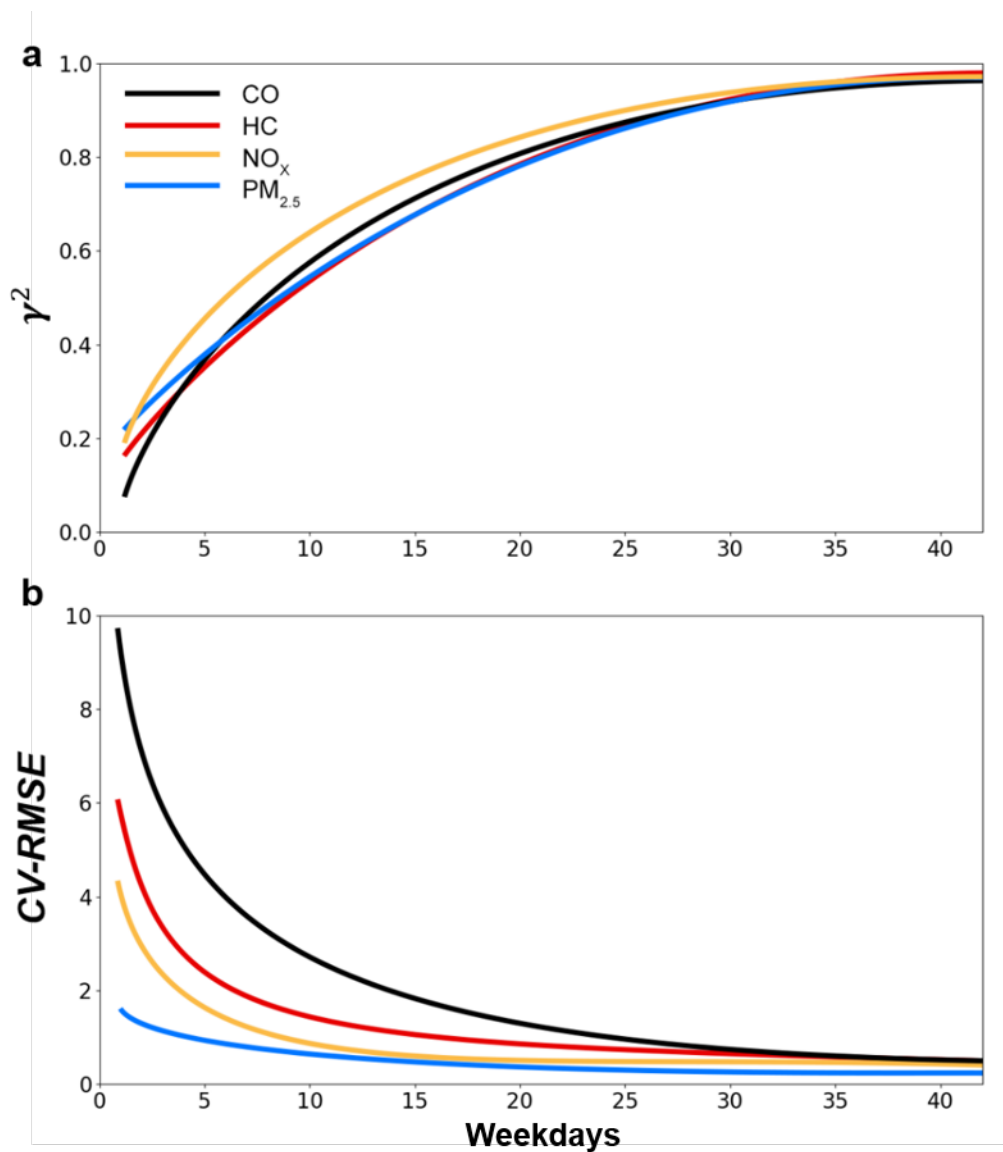
640

Figure 8. Scaling analysis through systematic subsampling. Using the systematic subsampling algorithm described in Section 2.4, we investigated the relationship between number of drive days and metrics of precision and bias. (a) Mean subsampled γ^2 versus the number of unique weekdays for CO, HC, NOx, and PM2.5. (**b**) Mean subsampled coefficient of variation of root mean squared errors (**CV-RMSE**) versus the number of unique weekdays for CO, HC, NOx, and PM2.5.

Table 1. Traffic control strategies. The detailed rules are presented spatially and temporally.

Traffic control strategy	Time scale	Space scale	Vehicle category	Rule
S1	Morning and evening rush hours during from Monday to Friday	Arterial and residential roads	All	For each weekday (from Monday to Friday), vehicles with specific tail numbers of the license plates were prohibited on the arterial and residential roads during the morning and evening rush hours (from 7:00 to 9:00 and from 16:30 to 18:30, Local Time). The prohibited tail numbers were 1 and 9 on Monday, 2 and 8 on Tuesday, 3 and 7 on Wednesday, 4 and 6 on Thursday, and 5 and 0 on Friday.
S2	Morning and evening rush hours during from Monday to Friday	Arterial and residential roads	All	The even-odd rule for the license plates was adopted over the arterial and residential roads on weekdays.
S3	All day	Highways	HDVs and HDTs	Both local registered and non-registered trucks were strictly prohibited all day long over the highways.
S4	All day	All roads	All	All kinds of vehicles complied with the even-odd rule of the license plates over the entire District.